Towards models of gravitational waveforms from generic binaries: A simple approximate mapping between precessing and nonprecessing inspiral signals

Patricia Schmidt,[1] Mark Hannam,[1] and Sascha Husa[2]

[1]*School of Physics and Astronomy, Cardiff University, Queens Building, CF24 3AA Cardiff, United Kingdom*
[2]*Departament de Física, Universitat de les Illes Balears, Crta Valldemossa km 7.5, E-07122 Palma, Spain*
(Received 30 July 2012; revised manuscript received 28 September 2012; published 27 November 2012)

One of the greatest theoretical challenges in the buildup to the era of second-generation gravitational-wave detectors is the modeling of generic binary waveforms. We introduce an approximation that has the potential to significantly simplify this problem. We show that generic precessing-binary inspiral waveforms (covering a seven-dimensional space of intrinsic parameters) can be mapped to a two-dimensional space of nonprecessing binaries, characterized by the mass ratio and a single effective total spin. The mapping consists of a time-dependent rotation of the waveforms into the quadrupole-aligned frame and is extremely accurate (matches >0.99 with parameter biases in the total spin of $\Delta\chi \leq 0.04$), even in the case of transitional precession. In addition, we demonstrate a simple method to construct hybrid post-Newtonian–numerical relativity precessing-binary waveforms in the quadrupole-aligned frame and provide evidence that our approximate mapping can be used all the way to the merger. Finally, based on these results, we outline a general proposal for the construction of generic waveform models, which will be the focus of future work.

DOI: 10.1103/PhysRevD.86.104063 PACS numbers: 04.20.Ex, 04.25.D−, 04.30.Db, 95.30.Sf

I. INTRODUCTION

The second-generation laser interferometric gravitational-wave detector Advanced LIGO is planned for first commissioning in 2014 and to reach design sensitivity in subsequent years [1–3]; Advanced Virgo [4,5] and Kagra [6] are expected to follow soon after. Current estimates of astrophysical event rates predict that the first direct detection of gravitational waves will occur in that time frame [7]. The coalescence of two black holes is among the strongest known gravitational-wave sources and a likely candidate for one of the first detections. The detection and subsequent analysis of gravitational waves rely strongly on the accuracy and completeness of theoretical waveform models. For black-hole binaries, this includes the inspiral, merger and ringdown of the final black hole, and current models combine information from analytic approximation methods and numerical-relativity (NR) simulations [8].

To date, a number of theoretical inspiral-merger-ringdown (IMR) waveform models exist for nonspinning binaries and configurations where the spin angular momentum is either aligned or antialigned with the orbital angular momentum (a summary of these models is given in Ref. [8]). But most astrophysical binary systems are expected to have arbitrary spin configurations, which lead to complicated precession effects. Although there does exist one preliminary precessing-binary IMR model [9], the modeling of generic binaries remains a serious challenge.

The complicated structure of precessing-binary waveforms suggests that in order to construct accurate IMR waveform models, we may need to produce numerical simulations that densely sample a seven-dimensional parameter space. At first glance, this does not seem feasible on the timescale of second-generation gravitational wave (GW) detectors (i.e., within the next ten years), although valiant efforts are underway [10].

In this paper we introduce an approximation that has the potential to dramatically simplify the modeling of precessing-binary waveforms. Motivated by the results of our previous work [11], we show that the seven-dimensional space of intrinsic physical parameters of generic precessing-binary waveforms can be mapped to a two-dimensional space of nonprecessing waveforms, parametrized by the mass ratio and an effective total spin parameter. The mapping consists of transforming the precessing-binary waveforms into a "co-precessing" frame of reference, described by three rotation angles $\{\gamma(t), \beta(t), \epsilon(t)\}$. This is the "quadrupole-aligned" (QA) frame that we introduced in Ref. [11]. The waveform modeling problem is then factorized into two much smaller problems: (1) the construction of a nonprecessing-binary model (and candidates for such a model already exist [12–14]) and (2) the construction of a model for the rotation angle functions $\{\gamma(t), \beta(t), \epsilon(t)\}$ with respect to the binary's seven physical parameters, which we expect can itself be further simplified. In this paper we do not address the (still very large) task of producing a model for the rotation angle functions, and we leave the behavior of the signal during the ringdown for future work. Here we restrict ourselves to an outline of the approximate mapping between precessing-binary and nonprecessing-binary waveforms and test its validity on a series of inspiral waveforms generated by post-Newtonian (PN) theory.

Generic binary systems undergoing quasicircular inspiral are characterized by nine intrinsic physical parameters: the binary's total mass $M = m_1 + m_2$, the mass ratio $q = m_2/m_1$ (we adopt the convention that $m_1 < m_2$), and

the six spin components $\vec{S}_1$ and $\vec{S}_2$. The total mass of the system sets the overall scale and can be factored out. The individual masses m_1 and m_2 are uniquely determined given M and q.

In the most simple cases, the two black holes are either not spinning, or their spin angular momenta are (anti-) aligned with the orbital angular momentum $\vec{L}$. In these cases the inspiral motion is confined to a fixed, time-independent plane. The orbital frequency of the motion then grows monotonically with time and, when the GW signal is decomposed into spin-weighted spherical harmonics, most of the emitted gravitational energy is contained in the dominant harmonics, the $(l = 2, |m| = 2)$-modes. In the most general configurations, however, the two black-hole spins are not aligned with the orbital angular momentum vector. Now the inspiral motion is no longer confined to a fixed plane. In these cases precession occurs, specifically two types: precession of the instantaneous orbital plane as well as precession of the spin vectors. The now far more complex motion is reflected in the emitted radiation in the form of strong amplitude modulations, which depend on the relative orientation of the binary toward the observer, and as a contribution to the binary's phase evolution. These effects are illustrated further in Sec. II A.

We have previously shown that precessing-binary waveforms take a far simpler form when transformed into the QA frame [11]. In a nutshell, the QA frame approximately follows the instantaneous orbital plane of the binary. In this frame the binary is essentially viewed "face-on" throughout the course of its evolution. Note that this frame corresponds to a corotating, accelerated frame of reference. In this "co-precessing" frame, the amplitudes of the waveform modes as well as their frequency evolution are significantly simplified and most of the energy is emitted in the $(l = 2, |m| = 2)$-modes, just as in a nonprecessing binary. In fact, in this accelerated frame the mode structure of a nonprecessing binary appears to be restored (see Fig. 12 in Ref. [11] for a NR example). It was this observation that suggested the idea that we pursue in this paper, that QA- and nonprecessing-binary waveforms may agree well in both amplitude *and* phase. Note that a related frame, defined by the direction of the Newtonian orbital angular momentum, was introduced in Ref. [15], along with the observation that the precession-induced phase oscillations can be removed in this "precessing frame." The key new result in this paper, beyond the use of the QA frame (which can be determined from the GW signal alone), is the simple mapping between precessing-frame waveforms and nonprecessing-binary waveforms, as we describe below.

In the context of gravitational-wave searches and parameter estimation, waveforms from different binary configurations are most strongly characterized by their phase evolution, i.e., their rate of inspiral. When the black holes are widely separated, their motion can be described well by PN methods, and in PN theory we see that the leading-order influence of the spin on the inspiral rate and the phase evolution is the spin-orbit coupling, which is due to a sum of the components of the black-hole spins parallel to the orbital angular momentum [16]. If the binary precesses, then the precession will introduce both secular and oscillatory changes in the phase, but in the QA frame, where the precession has been removed to some extent, we expect to recover the underlying orbital phase evolution, which will be similar to that for a nonprecessing binary. Since the leading-order spin effects on the phase arise from the total black-hole spin, it is possible to make an approximate parametrization of nonprecessing binaries by a single effective total spin parameter, $\chi_{\rm eff}$, and this idea has been used in both inspiral [17] and IMR [13] models. In this work we focus on inspiral PN models, and so we will use the same effective spin parameter as in Ref. [17]; see Sec. III. For complete IMR waveforms, other parametrizations have been found to work better [12,13], but in this work we restrict ourselves to PN inspiral waveforms.

Our hypothesis, then, is that precessing-binary waveforms can be approximately mapped to nonprecessing-binary waveforms, and that the equivalent nonprecessing-binary signal is parametrized by the mass ratio and $\chi_{\rm eff}$. It is the goal of this paper to quantify the accuracy of that approximation. Our approach is to consider a selection of PN inspiral precessing-binary waveforms, and to match them against a family of nonprecessing-binary signals, to determine the best-match value of $\chi_{\rm eff}$. We can then see how well these values agree with our expectation, and the level of agreement with the best-match waveform. We use PN waveforms because they allow us to study the long inspiral regime, and they are far more computationally convenient to produce than numerical simulations of only the last $\sim$10 orbits before merger.

In Sec. II A we will describe some of the general features of precessing-binary systems before giving a brief summary of the PN inspiral waveforms in Sec. II B. We provide a technical summary of the quadrupole-alignment procedure in Sec. II C. We perform our study of PN waveforms in Sec. III and demonstrate the efficacy of our approximate mapping not only for a large number of cases that exhibit simple precession, but also for an example configuration that undergoes transitional precession. In Sec. IV we show that the QA frame greatly simplifies the construction of hybrid PN-NR waveforms for precessing configurations and discuss the potential extension of our approach to full IMR waveforms. Finally, we sketch a procedure to construct generic IMR models and discuss the issues that must first be overcome.

II. PRECESSING-BINARY WAVEFORMS

A. General features

In this section we summarize the main features of precessing-binary systems and illustrate the effects of precession on the gravitational-wave signal. For a

comprehensive discussion of precessing-binary systems, we refer the reader to Refs. [16,18], which remain the standard references in the field.

In nonspinning or spin-aligned cases the normal to the orbital plane, i.e., the Newtonian orbital angular momentum $\hat{L}_N$, is well defined and does not evolve and provides a useful direction with which to characterize the dynamics. In the presence of precession, any such characteristic direction becomes time dependent. But one nearly fixed direction in the binary configuration does exist: the direction of the total angular momentum remains close to its limit when the binary has infinite separation. We denote this as the "asymptotic total angular momentum direction" $\hat{J}_{-\infty} \equiv \hat{J}(t \to -\infty)$. (We will use a hat to denote unit vectors.) This is analogous to standard Newtonian solid-body mechanics, where the system rotates about the axis defined by the total angular momentum, which is a natural fixed direction. This is still true for Newtonian and first-order post-Newtonian binary systems. When spin effects are included, starting at 1.5 PN order, and in full general relativity, this natural direction of rotation still exists, but it is no longer fixed. The direction of the total angular momentum is now time dependent. It evolves, but in cases with small precession, and for large separations, it describes a precession cone that is rather small compared to all of the other time-dependent directions, like the orbital angular momentum or the spin directions [19]. In a few special cases, where the orbital and spin angular momenta are nearly equal and opposite and the total angular momentum passes through zero during the inspiral, the direction of the total angular momentum changes rapidly; this is called transitional precession.

The complex dynamics in precessing systems is reflected in the gravitational-wave signal. The precession introduces amplitude modulations but also contributes to the phasing. Furthermore, the power contained in various gravitational-wave spherical harmonic modes, defined with respect to a fixed coordinate system, is significantly affected by precession, as power is transferred to the modes that were subdominant in the nonprecessing configurations. Nonetheless, since the GW signal is to first approximation produced by the acceleration of the two bodies in orbit, the bulk of the energy is emitted along the direction of the orbital angular momentum $\hat{L}$. This is the idea behind quadrupole-alignment: if we track the direction of the maximum energy emission, then we will also be tracking the orbital precession.

This also provides insight into the signal observed from a fixed direction. The orbital angular momentum $\hat{L}$ precesses around $\hat{J}_{-\infty}$, and on average we expect the bulk power to be radiated in the direction of $\hat{J}_{-\infty}$. This point is discussed in more detail in Ref. [20]. If a generic precessing binary now happens to be ideally oriented toward some static observer, i.e., the line of sight and $\hat{J}_{-\infty}$ coincide, only small amplitude modulations will be observed in the gravitational waveform, since the relative orientation between the observer and the least-precessing axis of the binary does not change much. On the other hand, if the observer's orientation does not coincide with this most stable axis, then they will observe strong modulations.

To illustrate this point, we consider a single-spin binary system with mass ratio 1:10, where the larger black hole has an initial spin of $\vec{\chi}_2 = (0.75, 0, 0)$ and the smaller one is nonspinning. We expect to see only very few oscillations from directions close to $\hat{J}_{-\infty}$. This is illustrated in Fig. 1: the first panel shows the real part of the post-Newtonian (2,2)-mode of the GW strain h (see Sec. II B for details) of the precessing binary as seen along the direction of the binary's initial total angular momentum. The second panel shows the real part of the (2,2)-mode for the same configuration, but for an observer whose line of sight does not coincide with the direction of the initial total angular momentum. In this case, the line of sight coincides with the direction of the Newtonian angular momentum at the beginning of the waveform. This direction varies with time and crosses the observer's line of sight after each precession cycle. The amplitude peaks are observed when the maximal emission direction points toward the observer.

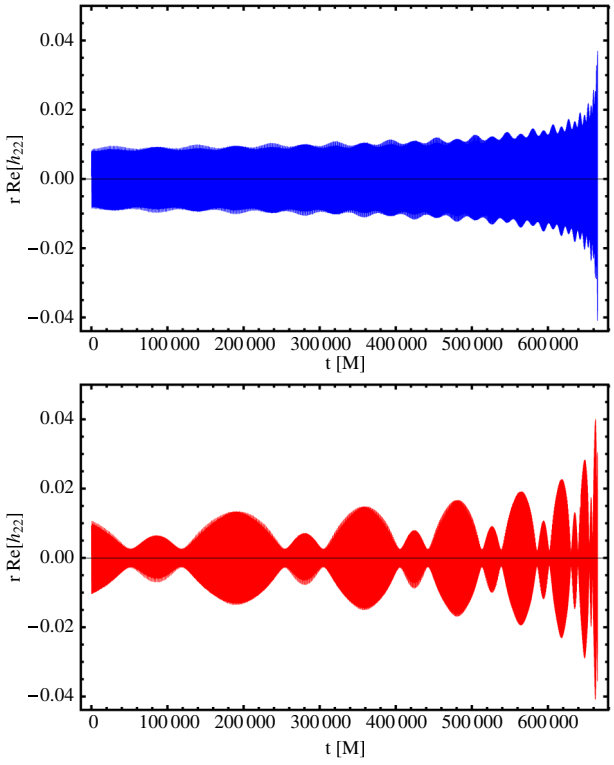

FIG. 1 (color online). The first panel shows the real part of the ($\ell = 2$, $m = 2$) mode with $\hat{J}$ initially aligned with $\hat{z}$, for the 1:10 binary described in the text. The second panel shows the same quantity, but now with $\hat{L}$ initial aligned with $\hat{z}$. It is clear that if we are searching for signals with a monotonically increasing amplitude (as with nonprecessing binaries), we may easily class the signal in the lower panel as a glitch in the data.

(Note that since the line of sight coincides with $\vec{L}$ at $t = 0$, the amplitude has a maximum at this time.)

The detectability of a signal in a matched-filter GW search can be estimated based on its best match against all of the theoretical signals in the template bank; the match is unity if the template bank contains precisely that signal, and is zero if the signal is orthogonal to all of the template-bank waveforms. (Match calculations will be described in more detail in Sec. III.) For the two waveforms shown in Fig. 1, the first has a match against a nonprecessing-binary template bank of over 0.97 (which means that more than 90% of such signals would be found in a search), while the second has a best match below 0.7, meaning that it would most likely either be missed, or classed as a glitch in the data. These illustrations provide a useful perspective on the results in Ref. [17], where it was shown that spin-aligned GW searches are very likely to miss a large number of generic signals at high mass ratios. We see that these signals are lost not simply because precessing-binary signals are very different from nonprecessing-binary signals. Rather, for some orientations they look very similar, but the fraction of those orientations decreases as the precession effects increase.

These examples demonstrate the dramatic difference in the precessing-binary waveforms with respect to relative orientation. But we have seen that even in the $\hat{J}_{-\infty}$ direction modulations remain in the waveform, and we will see in Sec. II C that these are further reduced when we go to the QA frame.

B. Post-Newtonian waveforms

In order to produce the precessing post-Newtonian inspiral waveforms used in this analysis, we evolved the full PN equations of motion, which were integrated using a MATHEMATICA package. In many studies of precessing binaries and in GW search work, it is common to use adiabatic inspiral models, for example the "SpinTaylor" equations, which are the precessing-binary extension of TaylorT4. But, in order to capture as much of the full physics as possible, we prefer to use instead an evolution of the full PN equations of motion, formulated as the Hamiltonian equations of motion in the standard Taylor-expanded form, as we have done previously [21–23]. More specifically, we use the nonspinning 3PN accurate Hamiltonian [24–26] (see also Refs. [27–29]) and the 3.5PN accurate radiation flux [30–32]. We add both leading-order [16,33–37] and next-to-leading-order [38–40] contributions to the spin-orbit and spin-spin Hamiltonians, and the spin-induced radiation flux terms as described in Ref. [41] (see also Refs. [16,37]). In addition we include the flux contribution due to the energy flowing into the black holes, which appears at the relative 2.5PN order, as derived in Ref. [42].

The precessing PN waveforms were then generated making use of the explicit formulae for the waveform modes $h_{\ell m}$ as given by Eqs. (B1) and (B2) in Ref. [43]. The expression for the (2,0)-mode was provided by G. Faye and the $(2, -m)$-modes where constructed according to Eq. (4.15) in Ref. [43]. The positions, momenta and spins of the masses were read off the full PN solution and used to generate the parameters for the construction of the precessing waveform modes h_{2m}. These modes contain only the leading-order spin contributions but higher-order corrections are contained in the dynamics, since the Hamiltonian is known to higher order (see above). Therefore, even if the $h_{\ell m}$ expressions were evaluated only at quadrupole-order, the waveforms would still show many features of precession, since the dominant contribution to the waveforms is from the motion itself. Note that the dynamical calculations are performed in the Arnowitt-Deser-Misner transverse-traceless gauge, while the mode expressions are written in the harmonic gauge. This inconsistency will introduce errors into the waveforms, but we do not expect these to be larger than those due to the neglect of higher-order PN contributions.

We have set up the source coordinate system as in Ref. [43], where $\hat{J}_0 = (0, 0, 1)$ and defines the total angular momentum direction at the initial separation. To achieve this, the PN initial data $\{\vec{q}, \vec{p}, \vec{S}_1, \vec{S}_2\}$ were rotated by applying a standard rotation matrix about the y- and z-axes in the Cartesian source frame. This is purely a convention as all of the physics is invariant with respect to rotations. The system was evolved for 15 M to reduce eccentricity (as done previously in numerical applications [21–23]), and then from an initial separation of $D_i = 40$ M down to a final separation of $D_f = 6$ M.

The orbital frequency of the motion is given by the general expression

$$\vec{\omega}_{\rm orb} = \frac{\vec{q} \times \dot{\vec{q}}}{\|\vec{q}\|^2}, \tag{2.1}$$

where $\vec{q}$ is the relative separation of the point masses and $\dot{\vec{q}}$ the relative velocity. The Newtonian orbital angular momentum is given by

$$\vec{L}_N = \mu(\vec{q} \times \dot{\vec{q}}), \tag{2.2}$$

where μ denotes the reduced mass

$$\mu = \frac{m_1 \cdot m_2}{m_1 + m_2}. \tag{2.3}$$

The general PN orbital angular momentum vector $\vec{L}$ is given by

$$\vec{L} = \vec{q} \times \vec{p}. \tag{2.4}$$

Note that $\vec{L}_N$ and $\vec{L}$ differ significantly in the case of precession since $\dot{\vec{q}}$ and $\vec{p}$ are no longer strictly parallel to each other, as explained in Refs. [11,16] unless the two masses m_1 and m_2 are far apart. In the case of precession, the directions of $\vec{L}$, $\vec{L}_N$, $\vec{S}_i$ and $\vec{J}$ are all time-dependent. We will see in Sec. III B, and in particular in the left panel of Fig. 6, an example that illustrates that during simple precession $\hat{J}$ evolves on a much smaller precession cone than the orbital angular momentum.

The Newtonian orbital angular momentum $\vec{L}_N$ is defined by its polar coordinates $\{\iota(t), \alpha(t)\}$, which are measured with respect to the z-axis of our Cartesian source system. The evolution of these two angles describes the dynamics of the instantaneous orbital plane. They are defined by

$$\iota(t) = \arccos\left(\frac{L_{Nz}}{\|\vec{L}_N\|}\right), \tag{2.5}$$

$$\alpha(t) = \arctan\left(\frac{L_{Ny}}{L_{Nx}}\right). \tag{2.6}$$

The total phase of the binary is then constructed from the following integral [43]:

$$\Phi(t) = \int_0^t (\omega_{\rm orb}(t') - \dot{\alpha}(t')\cos\iota(t'))dt'. \tag{2.7}$$

The physical interpretation of the integral is as follows: the phase seen by an observer on the z-axis (which is the axis that defines our mode decomposition of the GW signal) is a combination of the actual motion of the orbital plane and its projection onto the xy-plane of the source frame. This can be better understood if we first consider a simplified example, where ι is constant (the orbital plane is tilted by a fixed angle with respect to $\hat{z}$), and $\dot{\alpha}$ is also constant ($\vec{L}_N$ precesses around $\vec{J}$ with a constant frequency). Then we see that the average observed frequency of the objects' motion will be larger or smaller than $\omega_{\rm orb}$ depending on the sign of $\dot{\alpha}$. It is the phase from this observed frequency that Φ describes.

The symmetric and antisymmetric spin combinations are constructed directly from the solution data:

$$\vec{\chi}_s = \frac{1}{2}(\vec{\chi}_1 + \vec{\chi}_2), \tag{2.8}$$

$$\vec{\chi}_a = \frac{1}{2}(\vec{\chi}_1 - \vec{\chi}_2), \tag{2.9}$$

where the dimensionless spins $\vec{\chi}_i$ are defined from the spin angular momenta $\vec{S}_i$ of each black hole by

$$\vec{\chi}_i = \frac{\vec{S}_i}{m_i^2}. \tag{2.10}$$

Once all time-dependent dynamical parameters are constructed, the waveform modes, h_{lm}, are evaluated. These are most commonly derived by expanding the complex polarization h,

$$h = h_+ - ih_\times, \tag{2.11}$$

in the basis of spin-weighted spherical harmonics ${}^sY_{lm}$ with spin-weight $s = -2$ due to the nature of the gravitational field:

$$h_{lm} = \int h(\theta, \varphi)\,{}^{-2}Y^*_{lm}(\theta, \varphi)d\Omega, \tag{2.12}$$

where * denotes complex conjugation. For a nonprecessing binary this means that if the source frame was chosen such that $\hat{L}_N$ is parallel to $\hat{z}$, the quadrupole contributions are h_{22} and $h_{2,-2}$. For precessing binaries, $\hat{L}_N$ is not in general parallel to $\hat{z}$, and hence modes with $m \neq |2|$ appear even at quadrupole order. They only vanish when $\iota = 0$ and $\alpha = \pi$.

Schematically, the h_{lm}-modes can be written as

$$h_{lm}(t) = f(M, r, \mu, \omega_{\rm orb}, \iota, \alpha, \Phi, \vec{\chi}_s, \vec{\chi}_a). \tag{2.13}$$

The expressions are evaluated for a constant luminosity distance r, which is scaled out of our results. Figure 2 shows the magnitude of the (2,2)-mode for the same precessing case as described in Sec. I. Despite this being a strongly precessing case ($\vec{S} \cdot \vec{L} = 0$), long-timescale modulations are hardly noticeable. This is because a preferred frame was already chosen for the evolution, as described previously. Only an observer whose line of sight coincides with $\hat{J}_0$ will see a signal of this form. The appearance and strength of amplitude modulations strongly depends on the relative viewing angle, as illustrated in Sec. II A.

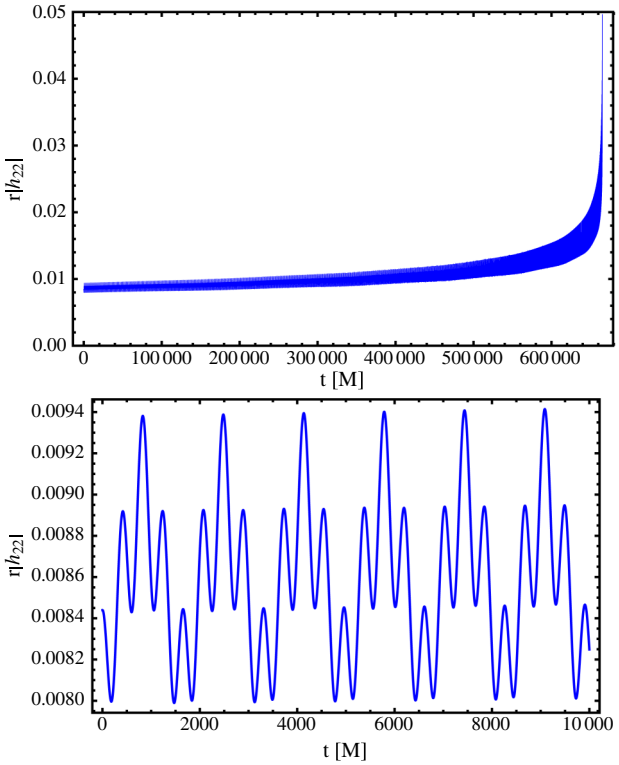

FIG. 2 (color online). The top panel shows the magnitude of the (2,2)-mode for the same strongly precessing case as in Fig. 1 over the whole length of the evolution, and over a length of the first 10000 M in the lower panel. The source frame was chosen such that $\hat{J}_0 \simeq (0, 0, 1)$, and $\vec{L}$ and $\vec{\chi}_2$ are initially orthogonal to each other with $\|\vec{\chi}_2\| = 0.75$; the smaller black hole is not spinning. The close-up of the waveform magnitude over a shorter timescale reveals strong amplitude modulations.

C. Quadrupole alignment

The idea of quadrupole alignment is to track the direction of the dominant radiation emission. This means that, to leading order, it follows the precessing motion of the instantaneous orbital plane. This allows us to significantly simplify the gravitational-wave signature by artificially removing the precession of the instantaneous orbital plane and describing the signal in a corotating way. In a previous study we have found evidence that the quadrupole-aligned direction actually tracks the full PN angular momentum direction, which differs slightly from the normal to the orbital plane. We will discuss this further in an upcoming publication [44].

We introduced the idea of the QA frame in Ref. [11] and illustrated its properties with reference to numerical-relativity waveforms. We also specified an explicit algorithm to determine the two time-dependent rotation angles $\{\beta(t), \gamma(t)\}$ that specify the direction that maximizes the amplitude of the $(\ell = 2, |m| = 2)$-modes. A third angle, $\varepsilon(t)$, which adjusts the phase, was ignored in our original prescription, but its importance was pointed out in Ref. [45], particularly in whenever β is close to zero and γ changes rapidly. An alternative algorithm to calculate these angles was later given in Ref. [46].

The alignment itself is based on the general transformation behavior of spin-weighted spherical harmonics under coordinate transformations. This allows us to find the instantaneous, average direction of maximal emission by transforming the $(\ell = 2, |m| = 2)$-modes and averaging over the dominant harmonics. This direction is uniquely defined by two angles, β and γ, which are determined by the maximization algorithm presented in Ref. [11]:

$$(\beta_{\rm MAX}, \gamma_{\rm MAX}) = \max_{\beta,\gamma} \sqrt{\|\tilde{h}_{22}(\beta, \gamma)\|^2 + \|\tilde{h}_{2,-2}(\beta, \gamma)\|^2}, \tag{2.14}$$

where $\tilde{h}_{22}$ and $\tilde{h}_{2,-2}$ are given by

$$\tilde{h}_{22}(\beta, \gamma) = \sum_{m'=-2}^{2} e^{-im'\gamma(t)} d^2_{m'2}(-\beta(t)) h_{2m'}(t), \tag{2.15}$$

$$\tilde{h}_{2,-2}(\beta, \gamma) = \sum_{m'=-2}^{2} e^{-im'\gamma(t)} d^2_{m',-2}(-\beta(t)) h_{2m'}(t), \tag{2.16}$$

where $d^2_{m'm}$ denote the Wigner d-matrices [47,48]. The maximization determines the two Euler angles $\beta_{\rm MAX}$ and $\gamma_{\rm MAX}$. In general, the transformation of spin-weighted spherical harmonics involves three degrees of freedom and, as noted in Ref. [45], the third angle can be provided by the analog of Eq. (2.7), given the other two angles:

$$\varepsilon(t) = -\int \dot{\gamma}_{\rm MAX}(t') \cdot \cos\beta_{\rm MAX}(t') dt'. \tag{2.17}$$

We may set $\varepsilon(0) = 0$ without loss of generality.

Once all three time-dependent angles $(\beta_{\rm MAX}, \gamma_{\rm MAX}, \varepsilon)$ have been determined, the dominant quadrupole-aligned mode can then be written as

$$h^{\rm QA}_{22}(t) = e^{-2i\varepsilon(t)} \sum_{m'=-2}^{2} e^{-im'\gamma_{\rm MAX}(t)} d^2_{m'2}(-\beta_{\rm MAX}(t)) h_{2m'}(t). \tag{2.18}$$

All other QA modes can be constructed as well, as long as the h_{lm}-modes for a given l are known. One may see that this transformation differs slightly from the one presented in Ref. [11]. This is because the numerical-relativity waveforms presented there are related to the PN waveforms in this work by an overall complex conjugation.

The three angles $\{\gamma, \beta, \varepsilon\}$ define a standard Euler rotation of the reference frame: a rotation by γ about the z-axis, followed by a rotation by β about the y-axis, followed by another rotation by ε about the (new) z-axis. This is important to bear in mind if we consider the reverse procedure to "wrap up" a QA waveform back into its original precessing-binary form. In that case, the reverse procedure consists of applying the rotations in the opposite order, i.e., the same procedure but with $\{\gamma, \beta, \varepsilon\} \to \{-\varepsilon, -\beta, -\gamma\}$.

Although we expect QA waveforms to be useful tools in standardizing the representation of precessing waveforms

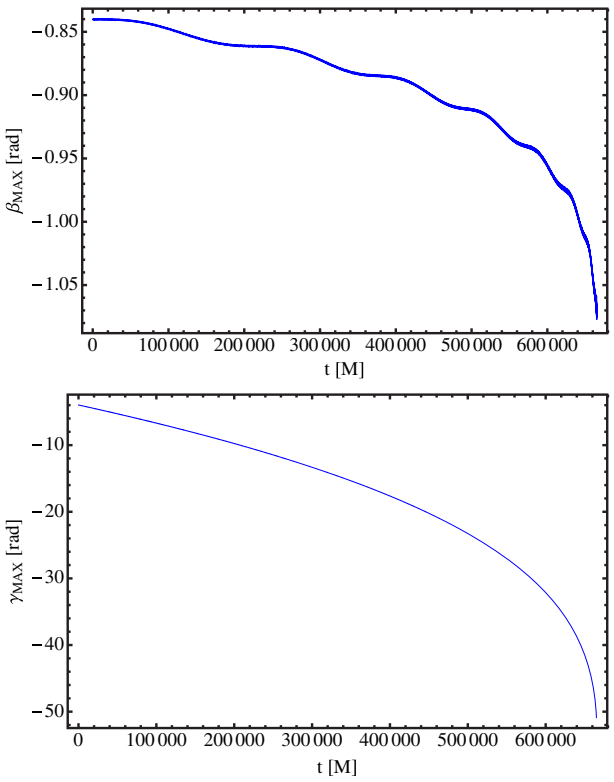

FIG. 3 (color online). The two panels show the angles found in an example of the maximization routine. The first panel shows the inclination angle $\beta_{\rm MAX}$ vs time, the second panel shows the azimuth $\gamma_{\rm MAX}$ vs time over the full length of the PN inspiral.

for comparison purposes (as in, for example, Ref. [49] for equal-mass nonspinning waveforms), and in waveform modeling, they do not correspond to a signal seen by a gravitational-wave detector. The QA waveforms are the waves as seen in a very specific accelerated "co-precessing" frame. One of the consequences of this frame choice is that the usual relationship $\Psi_4 = -\ddot{h}$ no longer holds, as can be seen by inspection of Eq. (2.18). Hence, in order to obtain quadrupole-aligned Weyl scalar modes, one has to construct the precessing modes first and then transform them into the quadrupole-aligned counterparts. Note also that the QA angles will differ slightly when calculated from either h or Ψ_4 (this point is also made in Ref. [50]; the Ψ_4 angles tend to be smoother than the h angles).

To leading PN order, the recovered angles correspond to the inverse Newtonian angles (ι, α), but higher order contributions in the wave amplitudes lead to a deviation from those angles, which is consistent with the results from the pure numerical analysis in Ref. [11]. From that work we expect the angles we find to correspond to the smooth evolution of $\hat{L}$ in the limit of a complete description. The angles found by the maximization routine are shown in Fig. 3. They deviate slightly from the inverse Newtonian ones $(-\iota, -\alpha)$ due to higher-order PN contributions to the mode amplitudes but this difference is not visible over the scale of the plots. If we were to use only the quadrupole contribution of the $h_{\ell m}$ expressions, then we would recover the direction of $\hat{L}_N$.

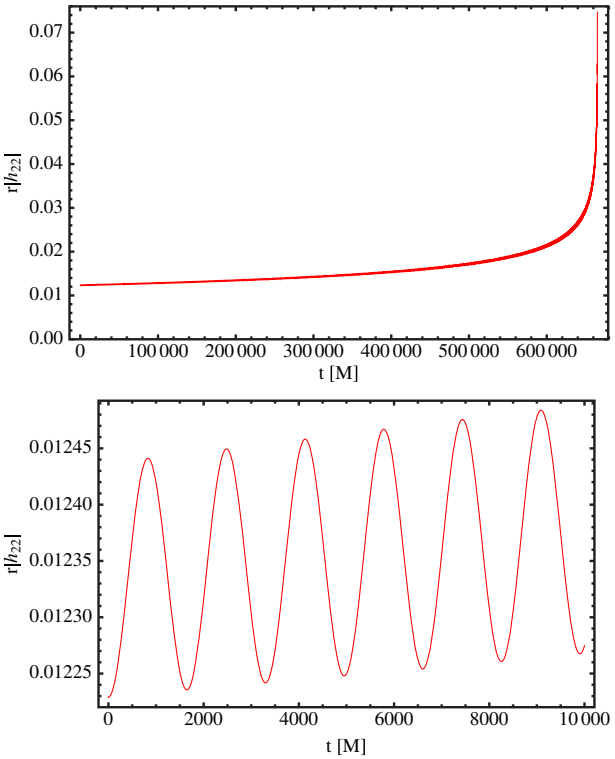

FIG. 4 (color online). QA magnitude for the $q = 10$ configuration considered in Figs. 1 and 2. The top panel shows the complete waveform, while the lower panel zooms in on the first 10000 M. We see that the oscillations in the amplitude have been reduced and simplified from those in Fig. 2.

Once the three Euler angles are determined, those are then used to reconstruct the QA modes. Figure 4 shows the quadrupole-aligned (2,2)-mode for the configuration shown in Figs. 1 and 2.

In the next section we will present a detailed study of how these simplified QA waveforms compare with corresponding nonprecessing cases.

III. RESULTS

The aim of this section is to test and quantify the accuracy of our hypothesis that generic inspiral signals can be mapped onto nonprecessing counterparts (see Sec. I). Numerical-relativity waveforms are too short for a real inspiral comparison and, moreover, it is computationally very expensive to produce a large number of accurate numerical precessing waveforms. Instead, we have restricted this analysis to PN waveforms to allow a more detailed study for a large subset of the precessing parameter space.

First, we will take a look at simple precession and consider a range of spin configurations for two mass ratios. The first is $q = 3$ and includes the configuration of the numerical case that we studied in Ref. [11]. The second is $q = 10$, motivated by the observation that precession effects become more significant for higher mass ratios; see, for example, Eq. (2.11) in Ref. [16], and the results presented in Ref. [17]. We will show that the mapping works extremely well; the nonprecessing waveforms that agree best with each QA-transformed precessional configuration follow closely the $\chi_{\rm eff}$ parameter that we discussed in Sec. I (and will elucidate further below) and agree with them with matches above 0.99. Finally, as the most challenging test of our hypothesis, we look at a case of transitional precession.

This study covers only a small range of the full precessing-binary parameter space, but the configurations were carefully chosen to test the hypothesis for varying spin magnitudes and for two mass ratios within the range that is likely to be treated in IMR models in the near future, i.e., cases which can also be realized in current numerical simulations to high accuracy.

From the PN expressions for the phase evolution of the binary [16], we see that the dominant spin contribution is proportional to the projection of each spin vector onto the orbital angular momentum, $(\vec{S}_i \cdot \vec{L})$. We characterize the degree of spin-alignment with κ_i, which is defined as the angle between $\vec{S}_i$ and $\vec{L}$,

$$\kappa_i = \arccos\left(\frac{\vec{S}_i \cdot \vec{L}}{\|\vec{S}_i\|\|\vec{L}\|}\right). \tag{3.1}$$

When the spin interaction is restricted to the leading order spin-orbit coupling and radiation reaction is switched off,

each κ_i is conserved and is a constant of the motion [16]. When radiation reaction is included and, to a lesser degree, when higher order spin interactions are included, κ_i has been observed to show only small variation in time.

The agreement or disagreement between two waveforms is mainly due to their phasing. If the inspiral rate is significantly different, two waveforms are not expected to agree very well. For the QA waveforms, the precession of the orbital plane has been factored out, but the physical spins are, of course, present and contribute to the phase evolution. Thus, in general, we expect the best comparison waveform to be from a spinning-black-hole binary. At leading PN spin-order, where only the leading order spin-orbit terms contribute, each spin contribution is proportional to $\cos\kappa_i$, and thus by looking at the leading-order terms, we expect that all waveforms with $\cos\kappa_i = 0$ map onto nonspinning counterparts, while all waveforms with $\cos\kappa_i \neq 0$ map onto spinning waveforms, which can be parametrized by an effective total-spin parameter. This 2-part leading-order spin term can be represented by a *single* reduced spin parameter [17]:

$$\chi_{\rm eff} = \chi_{sz} + \frac{(m_1 - m_2)}{m}\chi_{az} - \frac{76\eta}{113}\chi_{sz}, \qquad (3.2)$$

where η is the symmetric mass ratio. Note that this parameter is not the same effective spin parameter as introduced in Ref. [36]. In this work the effective total spin used *is* the reduced spin parameter as defined by Eq. (3.2).

In our study the nonprecessing-binary comparison modes were parametrized by $\vec{\chi}_1 = \vec{\chi}_2 = (0, 0, \chi)$. For each of these cases we have $\chi_{\rm eff} = \chi(1 - 76\eta/113)$.

The first set of configurations was chosen such that $\kappa_i = 0$ for the spinning hole, yielding an effective spin of zero. The second set was chosen such that all configurations have the same theoretical effective spin of $\chi_{\rm eff} = 0.5$, but with varying $\kappa_1 = \kappa_2$. The details are listed in Tables I and II. The PN comparison family with (anti-)aligned spins was generated by the same method as the precessing ones, solving the full PN equations of motion and using the same $h_{\ell m}$ expressions [43], where $\alpha = \pi$ and $\iota = 0$. This ensures that the results are not contaminated by differences due to the choice of the PN approximant.

TABLE I. PN configurations with constant $\kappa_i = 90°$ for the spinning hole and varying spins. The best matches, not necessarily for the predicted $\chi_{\rm eff} = 0$ but for the values displayed in column 4, are all well above 0.999 for $q = 3$ and above 0.995 for $q = 10$. $\mathcal{M}_0$ denotes the match with the counterpart waveform that has $\chi_{\rm eff} = 0$. The last two columns show the best match for two potential Advanced LIGO noise curves, evaluated for a $20M_\odot$ binary. For all cases the best match is above 0.999 for both detector noise curves.

q	$\vec{\chi}_1$	$\vec{\chi}_2$	$\chi_{\rm BM}$	$\mathcal{M}_0$	$(\chi_{\rm BM})_{\rm early}$	$(\chi_{\rm BM})_{\rm zdethp}$
3	(0,0,0)	(0.75,0,0)	0.02	0.9815	0.02	0.02
3	(0.75,0,0)	(0,0,0)	0.00	0.9997	0.00	0.00
3	(0.75,0,0)	(0.75,0,0)	0.03	0.9576	0.04	0.03
10	(0,0,0)	(0.75,0,0)	0.03	0.8209	0.03	0.03
10	(0.75,0,0)	(0,0,0)	0.00	0.9999	0.00	0.00
10	(0.75,0,0)	(0.75,0,0)	0.03	0.8075	0.03	0.03

TABLE II. PN configurations with the same effective spin value $\chi_{\rm eff} = 0.5$ but varying $\kappa_1 = \kappa_2$ for the two mass ratios 1:3 and 1:10. $\chi_{\rm BM}$ denotes the effective $\chi_{\rm eff}$-value yielding the best match. In all cases the best matches are above 0.999 for $q = 3$ and above 0.997 for $q = 10$. $\mathcal{M}_{0.5}$ denotes the match with the counterpart waveform that has $\chi_{\rm eff} = 0.5$. Column 5 lists the match for the predicted $\chi_{\rm eff}$-value. The last two columns show the best match for two potential Advanced LIGO noise curves, evaluated for a $20M_\odot$ binary.

q	$\vec{\chi}_1 = \vec{\chi}_2$	$\kappa_1 = \kappa_2$	$\chi_{\rm BM}$	$\mathcal{M}_{0.5}$	$(\chi_{\rm BM})_{\rm early}$	$(\chi_{\rm BM})_{\rm zdethp}$
3	(0.050,0,0.572)	5°	0.50	0.9998	0.50	0.50
3	(0.101,0,0.572)	10°	0.50	0.9998	0.50	0.50
3	(0.208,0,0.572)	20°	0.50	0.9992	0.51	0.50
3	(0.330,0,0.572)	30°	0.51	0.9975	0.51	0.51
3	(0.480,0,0.572)	40°	0.52	0.9917	0.52	0.52
3	(0.682,0,0.572)	50°	0.52	0.9719	0.52	0.52
10	(0.093,0,0.529)	10°	0.50	0.9986	0.50	0.50
10	(0.193,0,0.529)	20°	0.50	0.9996	0.50	0.50
10	(0.306,0,0.529)	30°	0.50	0.9965	0.51	0.50
10	(0.444,0,0.529)	40°	0.51	0.9771	0.51	0.51
10	(0.631,0,0.529)	50°	0.52	0.8925	0.53	0.52

The agreement between two waveforms can be quantified by a single number, the *match* $\mathcal{M}$, which corresponds to a noise-weighted inner product (overlap) between them [51]. Since QA waveforms are not in an inertial (detector) frame, and we are interested in quantifying the difference between two waveforms independently of a detector, we primarily use the white-noise spectrum $S_n(f) = 1$. Match calculations are performed in the frequency domain and hence the Fourier transforms of the time-domain waveform modes have to be computed first. The best match between two frequency-domain waveforms $h_1(f)$ and $h_2(f)$ is defined as their normalized inner product maximized over time and phase shifts (Δt and $\Delta\phi$):

$$\mathcal{M} = \max_{\Delta t, \Delta\phi} \frac{\langle h_1|h_2\rangle}{\sqrt{\langle h_1|h_1\rangle\langle h_2|h_2\rangle}}, \qquad (3.3)$$

where the inner product is defined by

$$\langle h_1|h_2\rangle := 4\,{\rm Re}\left[\int_{f_{\rm min}}^{f_{\rm max}} \frac{\tilde{h}_1(f)\tilde{h}_2^*(f)}{S_n(f)}\,df\right]. \qquad (3.4)$$

In our examples the PN waveforms are defined in the frequency range $fM \in [0.0018, 0.01]$. The upper frequency corresponds to $M\omega \approx 0.06$, which is typical of the frequency at which we would start using NR results in full IMR hybrids; in this study we are not interested in the performance of the PN waveforms beyond that

frequency. Since the matches are calculated with a flat noise spectrum, they are independent of the binary's mass.

Although the QA waveforms are not in a detector's frame of reference, it is also instructive to calculate matches with respect to realistic detector noise curves. In this case different choices of binary mass correspond to giving extra weight to different frequency ranges in the waveforms, and provide a more stringent test on the robustness of our results. We repeated the match calculation for every configuration with the early Advanced LIGO [52] and the zero-detuned high-power [53] noise curves. The matches were calculated for masses between $20M_\odot$ and $50M_\odot$ in the frequency range between 20 Hz and 8 kHz.

The idea of the comparison is to find the nonprecessing waveform as a function of χ that gives the best match with each QA waveform of our study. If our hypothesis holds, then the best-match spin $\chi_{\rm BM}$ will be close to the effective spin $\chi_{\rm eff}$. We present our results in the following subsections.

A. Simple precession

The first two sets of PN configurations are cases of simple precession. For most arbitrary binary configurations, simple precession will occur and only a small set of configurations will undergo "transitional precession," as it requires fine-tuned physical parameters (see Ref. [18] and Sec. III B below). In the case of simple precession, the total spin angular momentum $\vec{S}$ precesses around the orbital angular momentum vector $\vec{L}$ and both of these vectors precess around the centre of the rather small precession cone described by $\vec{J}_0$. This is illustrated in the left panel of Fig. 6.

Each precessing time-domain waveform was generated with respect to a source frame where $\hat{J}_0$ is initially parallel to the z-axis. The quadrupole-alignment algorithm was then applied to determine the time series of the two Euler rotation angles $\{\beta_{\rm MAX}(t), \gamma_{\rm MAX}(t)\}$. Given those, the third angle, $\varepsilon(t)$, was determined and Eq. (2.17) applied to reconstruct the time-domain quadrupole-aligned (2,2)-mode.[1]

The first set of configurations tests the mapping hypothesis for a vanishing proposed theoretical effective spin $\chi_{\rm eff} = 0$, for various spin configurations for the two mass ratios 1:3 and 1:10. The results in Table I suggest that the hypothesis works very well for single-spin systems with only the smaller black hole spinning. In these cases, we obtain best matches ≥ 0.99 for the theoretical $\chi_{\rm eff}$-value for both mass ratios. In the reversed cases, i.e., now the larger black hole is spinning, the maximal matches are still ≥ 0.99 but we see a small parameter bias of $\Delta\chi = 0.02$. If both black holes are spinning with the same spin magnitude and the spins initially parallel to each other ($\kappa_1 = \kappa_2$), the parameter bias increases slightly to $\Delta\chi = 0.03$. Note that in all of these cases the match has a sharp peak at its maximum, but the match at the theoretical $\chi_{\rm eff}$-value is well above 0.97 in many cases.

The results do not change appreciably when the calculations are repeated with the Advanced LIGO noise curves. The matches improve slightly as the mass is increased, but so does the bias in $\chi_{\rm eff}$. However, the bias never increases by more than $\Delta\chi = 0.01$. The results for the $20M_\odot$ bin are displayed in the last two columns of Tables I and II. We would like to emphasize again that QA waveforms are *not* in a detector frame: the matches using the detector noise curves are only to rule out the possibility of spurious results with the white-noise curve.

The second set was chosen such that all configurations have the same theoretical $\chi_{\rm eff}$-value, but that the amount of precession changes due to a varying $\kappa_1 = \kappa_2 \equiv \kappa$ angle. All configurations in this set are equal spinning, i.e., the spins are initially equal in magnitude and parallel to each other. The results are given in Table II. We see for both mass ratios $q = 3$ and $q = 10$ that the best-match χ_{BM} agrees with $\chi_{\rm eff}$ for small κ. A bias appears as κ increases beyond 30°, but is again never more than $\Delta\chi = 0.02$.

It is important to note that the parameter that describes the rate of inspiral, i.e., the phasing of the binary, is given by Eq. (3.2) and that the geometric quantity that defines the amount of precession is quantitatively described by the spin components perpendicular to $\vec{L}$, which are proportional to $\sin\kappa_i$. We have looked at various other cases with varying relative azimuth angle between the spin vectors as well as varying relative inclination between $\vec{S}_1$ and $\vec{S}_2$, i.e., $\kappa_1 \neq \kappa_2$. For equal spin magnitudes we find that the azimuth has no effect on the best-match χ_{BM}. For unequal κ_i but equal spin magnitude we find that the best-match bias increases with increasing κ_i but that the relative inclination angle between the two spin vectors does not have a significant influence on the results.

The approximation that $\chi_{\rm eff}$ is constant becomes less accurate as the binary approaches merger. Remarkably, the effective spin value associated with the initial $\chi_{\rm eff}$-value seems to characterize the best-match nonprecessing-binary system in all cases. Even when using detector noise curves and choosing masses such that the late inspiral (when $\chi_{\rm eff}$ changes fastest) is in the most sensitive part of the detector band, the best-match $\chi_{\rm eff}$ varies by only $\Delta\chi \leq 0.04$ from the value predicted by our hypothesis. However, it is likely that when we move to full IMR configurations, some other appropriate effective total spin will be more appropriate, as was found for the full IMR waveforms in Ref. [12].

When interpreting these results, one should bear in mind that the phasing of a PN waveform can change significantly with respect to the choice of PN approximant. The matches that we calculated between QA and nonprecessing waveforms are in general far better than those between, for example, the same nonprecessing configuration produced with TaylorT1 and TaylorT4; see Fig. 6 in Ref. [54]. In this

[1]Higher modes can be reconstructed as well but here we consider only the dominant harmonic in the match calculations.

sense, our approximation can be considered to hold, well within the level of accuracy of our PN waveforms.

We also emphasize once again that the QA waveforms do not correspond to the waveforms as seen by a detector, since the QA frame is accelerating, and would not be directly employed in a GW search; the matches as shown therefore do not constitute a study of the efficacy of these waveforms for either searches or parameter estimation. What they do tell us, however, is that if we were to take the nonprecessing waveforms used in this study and apply the reverse QA procedure to them, i.e., ''wrap them up'' into mock precessing waveforms, using the inverse QA angles calculated for each of these configurations, then we would expect them to agree well with the original precessing-binary waveforms. This study also suggests that if we were to construct a waveform model from ''wrapped up'' nonprecessing waveforms, then it is possible that this model could be used to measure the effective total spin $\chi_{\rm eff}$ with only a small bias. However, the true behavior of such a model in a parameter estimation exercise requires an exhaustive study that is beyond the scope of this paper.

To back up this claim, we performed the following exercise: from the first case in Table I we took the $\chi_{\rm eff}$ waveform, which is nonspinning $q = 3$, and wrapped it up with the reverse QA angles that we calculated for the $\{q = 3, \chi_1 = 0, \chi_{2,x} = 0.75\}$ configuration. The resulting waveform is shown in Fig. 5; we have plotted the absolute value of the GW strain, constructed from all $\ell = 2$-modes, at an arbitrarily chosen inclination of 2.8 rad from the initial direction of the total angular momentum, $\hat{J}_0$. Also shown is the same quantity for the ''true'' precessing-binary waveform, and for comparison we also show the original nonprecessing-binary waveform, constructed from only the ($\ell = 2$, $|m| = 2$)-modes. We see that the twisted-up, nonprecessing-binary waveform captures the main features of the amplitude of the true precessing-binary waveform extremely well; how well the phases agree can be judged by calculating the match between the two waveforms. This we did, once again over the frequency range of $fM \in [0.0018, 0.01]$. Note that now we *are* considering waveforms as they would be observed in a detector.

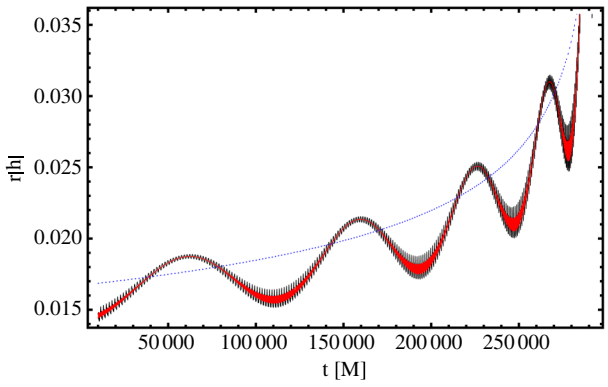

FIG. 5 (color online). The absolute value of the GW strain for a precessing binary, as viewed at an arbitrary inclination of 2.8 rad from $\hat{J}_0$. The signal includes all $\ell = 2$-modes. The true signal (black) has the finer structure; the signal with the lower-amplitude high-frequency oscillations (red) was generated by twisting a nonspinning $q = 3$ waveform with the inverse QA angles. The dotted line shows the amplitude of the original nonspinning waveform.

We find that the match between the true precessing-binary waveform and the mock-precession waveform have a match greater than 0.97 for all masses and binary orientations. By contrast, the match between the unmodified nonprecessing $q = 3$ waveform and the true precessing waveform is below 0.97 even for the best-performing orientation. These results provide an important cross-check that we can indeed mimic the original PN precessing-binary signal by suitably transforming the signal from a nonprecessing binary.

As an aside, note that there is one mode of the precessing-binary signal that we cannot fully model in this way, the ($\ell = 2$, $m = 0$)-mode. In the nonprecessing waveforms, the (2,2)- and (2, −2) modes are complex conjugates of each other. When this is true, the transformed (2,0)-mode will always be real. This can be seen from inspection of Eq. (2.18). But in the true precessing-binary waveform the (2,0)-mode has real and imaginary parts; it is straightforward to produce an example to illustrate this from Sec. IV of Ref. [43]. In order to capture these effects, we would need to break the symmetry between the nonprecessing $h_{\ell m}$-modes, which would require that our model include unequal spins; this is, therefore, one limitation of a single-effective-spin model. In practice, however, the relative signal power in the imaginary part of the (2,0)-mode (that part that our model cannot reproduce) will always be small, and we expect the other errors in this approximate waveform, for example in the phasing, will be more significant in practice.

B. Transitional precession

In the previous section we have seen that our mapping works extremely well in cases of simple precession; in fact it can be considered to be an exact mapping within the error bars of the PN phasing. In this section, we demonstrate that it also works in the more extreme case of transitional precession [18]. This second type of precession occurs when $\vec{L}$ and $\vec{S}$ are almost opposite and equal in magnitude and so $|\vec{J}|$ is small. During the inspiral, the magnitude of $\vec{S}$ hardly changes but since orbital angular momentum is radiated away, the magnitude of $\vec{L}$ decreases with time. With the appropriate choice of parameters, the total angular momentum $\vec{J}$ is initially small and positive, but due to the loss of orbital angular momentum, decreases until it crosses the xy-plane of the Cartesian source frame, where it

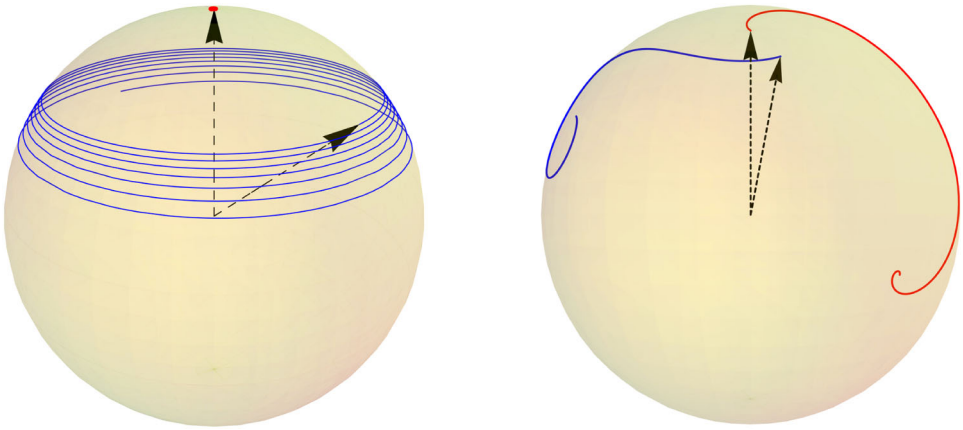

FIG. 6 (color online). Evolution of $\vec{J}$ (red) and $\vec{L}$ (blue) plotted on the unit sphere, where $\vec{J}$ is initially aligned with the direction (0,0,1). The left panel shows the evolution of these two directions for a case of simple precession. The precession cone described by $\hat{J}$ is very small in comparison to the one described by $\hat{L}$, and appears on the figure as only a dot at the end of the vertical arrow. The right panel shows the same characteristic directions for a case of transitional precession. In this case $\vec{J}$ clearly moves along the unit sphere away from its initial direction (to the right side of the sphere) and separates from $\vec{L}$, which moves to the left side of the sphere in the figure.

changes sign. See Ref. [18] for an extensive discussion of transitional precession.

As opposed to simple precession, where $\hat{J}_0$ represents the least evolving axis in the binary's geometry, this direction changes significantly during the transitional phase, as shown in Fig. 6. In order to test the validity of our precessing $\rightarrow$ nonprecessing mapping for a transitional-precession case, we have chosen one specific configuration with PN parameters $q = 10$, initial separation $D_i = 53$ M, and initial spins $\vec{\chi}_1 = (0, 0, 0)$ and $\vec{\chi}_2 = 0.65 \cdot (0, -\sin(3°), -\cos(3°))$. This is a single-spin configuration, where the initial spin is 3° from complete antialignment and the generated inspiral waveform is about 2×10^6 M long, terminating at a final separation of $D_f = 6$ M.

It is worth mentioning that in order to produce a transitional phase, the parameters have to be fine-tuned such that $\vec{J}$ changes sign. If $\vec{S}$ and $\vec{L}$ were completely antialigned, no precession would occur at all. The transitional phase is not brief: it takes up most of the duration of the inspiral that we have calculated, and, as noted in Ref. [18], cases where a binary undergoes transitional precession within the sensitivity band of ground-based detectors are expected to be very rare.

The dramatic change of the direction of $\vec{J}$ is reflected in the GW signal and the transitional waveforms in the standard source frame look particularly distorted when the total angular momentum crosses the xy-plane, as is shown in Fig. 7.

We do not expect any of these features to be present in the quadrupole-aligned waveform, since we now track the direction of dominant emission, and this is completely independent from any asymptotic direction of $\vec{J}$. We see in Fig. 7 that this is indeed the case. The angles found by the maximization routine are shown in Fig. 8. The zero-crossing of the total angular momentum occurs at $t = 1.587 \times 10^6$ M, which is indicated in the figures with a vertical line.

If our hypothesis were correct, then the QA waveform would be very close to a nonprecessing waveform with $\chi_{\rm eff} = -0.572$, from Eq. (3.2). As before, we compared the QA mode with a series of nonprecessing waveforms with varying spin parameter to locate the nonprecessing configuration that agrees best with the QA waveform. We find the best match to be 0.998 for a spin antialigned waveform with effective spin parameter $\chi_{\rm eff} = -0.576$. This is remarkably close to the theoretically expected value, with a bias of only $\Delta\chi = 0.004$!

On the other hand, naively using the nonaligned transitional-precession waveform and calculating the matches with the same comparison waveforms gives the

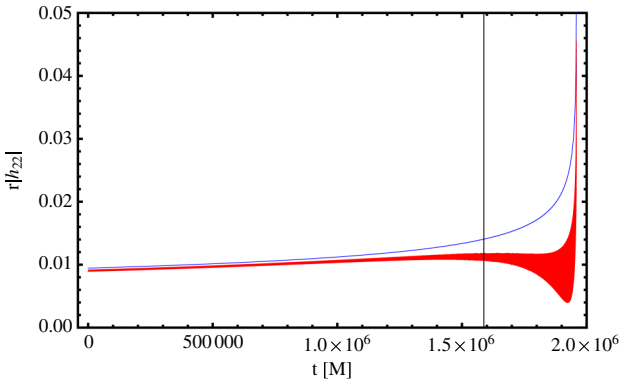

FIG. 7 (color online). The panel shows the magnitudes of the (2,2)-modes for the transitional precession case before (red; lower curve) and after (blue; upper curve) the quadrupole alignment was applied. The change of the direction of $\hat{J}$ at $t = 1.587 \times 10^6$ M is indicated by the vertical line. A strong modulation is introduced into the original waveform at that time, which is completely removed after quadrupole alignment.

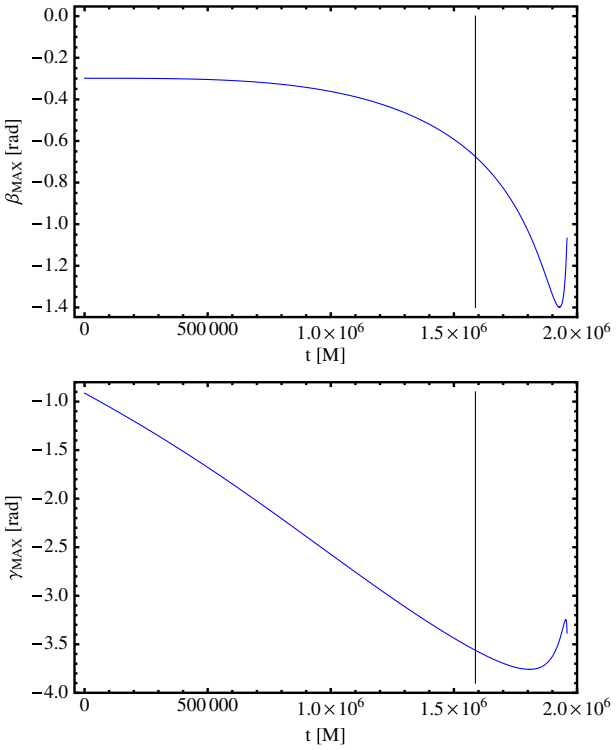

FIG. 8 (color online). The two panels show the two Euler angles β and γ determined by the quadrupole-alignment procedure for the transitional case. The time when the z component of $\vec{J}$ changes sign is indicated by the vertical line.

same effective spin value, since the phase is dominated by the inspiral rate, but yields a best match of only 0.940. Note also that this is for the (2,2)-mode as seen from only one orientation; for many other orientations that matches are likely to be far worse.

This example demonstrates that even in the case of transitional precession, our method proves to be accurate (expected $\chi_{\rm eff}$-value) and robust ($\mathcal{M} > 0.99$) for mapping precessing waveforms onto single-spin-parametrized nonprecessing-binary waveforms.

IV. PN-NR HYBRID WAVEFORMS

So far we have discussed only PN inspiral waveforms. To produce complete waveforms that include the late inspiral, merger and ringdown, we need to include results from NR simulations. In this section we will show how the quadrupole-alignment procedure simplifies the production of hybrid PN-NR waveforms.

A variety of methods have been introduced to construct hybrid waveforms for nonprecessing configurations [13,55–59], and see Ref. [54] for a unified summary of the methods in use. In all methods the PN and NR waveforms are aligned at some time, or over a time or frequency window, and then blended together. Such waveforms have been used to produce phenomenological waveform models [12,13,56,57,60], and are now also being used to test GW search and parameter estimation tools [54]. A number of studies have also been performed on the length requirements of NR waveforms in order to produce sufficiently physically accurate hybrids [59,61–63] and these also include estimates of the influence of errors and ambiguities in the hybridization process on the physical fidelity of the final waveform.

The construction of hybrids for precessing-binary configurations is more complex: not only do the time and phase of the PN and NR waveforms have to be aligned but also, to some extent, the orientations of the spins and orbital plane must agree as well. For the precessing-binary hybrids that were used in Ref. [12], the hybrid waveforms were constructed by matching the NR waveforms with PN waveforms computed from the same PN evolution that was employed to construct the initial data for the NR simulations. This technique ignores mismatches in the binary orientation and physical parameters due to the emission of junk radiation [64,65] and gauge changes [66,67] in the early stages of an NR simulation, although these effects are expected to be small; see Ref. [13] for a detailed discussion of this point in the context of nonprecessing-binary hybrids.

These complications can be avoided through the use of QA waveforms. The PN and NR waveforms, both converted to the QA frame, can now be aligned exactly as in the nonprecessing cases. In order to reverse the QA process, it is also necessary to align the QA angles $(\beta, \gamma, \varepsilon)$, but this is straightforward, as we show below.

In the next section we will outline how we produce a QA hybrid for the precessing-binary waveform that we used in Ref. [11]. This corresponds to the first configuration discussed in Table I: $q = 3$, $\chi_1 = 0$, $\chi_2 = 0.75$, and $\vec{S}\cdot\vec{L} = 0$. Having produced the QA hybrid, we will examine where our nonprecessing-binary mapping hypothesis breaks down as we approach merger. That the hypothesis must break down is clear, because the spin of the final merged black hole will be influenced by the black-hole spins in a way that the orbital phase evolution is not, and the mass and spin of the final black hole will *not* be the same as that for the corresponding nonprecessing inspiral configuration.

A. Construction of QA hybrids

A QA hybrid can be produced by making use of the same procedure as for a nonprecessing-binary hybrid. We will briefly summarize the method that we used.

We start with a PN and an NR waveform, each for the same physical configuration. The last requirement is achieved to good approximation by using results from the PN evolution to produce the initial parameters for the NR evolution. The PN and NR waveforms are then put into the QA frame by the procedure described in Sec. II C. We will produce a hybrid of Ψ_4, and note that, since the QA frame is noninertial, we cannot produce $\Psi_4^{\rm QA}$ by taking two time derivatives of $h^{\rm QA}$. We must first produce the

$\Psi_{4,2m}$-modes from the original precessing-binary GW-strain modes, h_{2m}, and apply the QA algorithm to $\Psi_{4,2m}$.

We then choose a matching frequency ω_m, and locate the times $t_{\rm PN}$ and $t_{\rm NR}$ when each waveform passes through that frequency. For our $q = 3$ configuration, $\omega_m = 0.07$. We align the PN and NR frequencies around that time such that both $\phi_{\rm PN}(t_{\rm PN}) = \phi_{\rm NR}(t_{\rm NR})$ and $\omega_{\rm PN}(t_{\rm PN}) = \omega_{\rm NR}(t_{\rm NR}) = \omega_m$. The hybrid waveform is then produced by blending together $\Psi^{\rm QA}_{4,\rm PN}$ and $\Psi^{\rm QA}_{4,\rm NR}$ with a linear transition function of width $\Delta t = 200$ M around the matching frequency. The final waveform is then

$$\Psi^{\rm QA}_{4,\rm hyb}(t) = a_- \Psi^{\rm QA}_{4,\rm PN}(t - t_{\rm PN}) + a_+ \Psi^{\rm QA}_{4,\rm NR}(t - t_{\rm NR}), \qquad (4.1)$$

where $a_\pm = (\Delta t/2 \pm t)/\Delta t$ when $t \in [-\Delta t, \Delta t]$ and zero or one otherwise, and the time has been shifted such that $t = 0$ coincides with the point at which $\omega = \omega_m$. This constitutes the QA hybrid. Figure 9 shows the real part of Ψ_4 around the time where the matching was performed, which is at $t = 0$. The figure shows the PN and NR waveforms, as well as the final hybrid, and we see that the matching between the PN and NR waveforms is smooth.

To convert this into a physical precessing-binary hybrid, we also require hybrids of the QA angles $\{\beta(t), \gamma(t), \epsilon(t)\}$. These are produced as follows. The two angles $\{\beta(t), \gamma(t)\}$ define a vector $\vec{n}(t) = \{\sin(-\beta(t))\cos(-\gamma(t)), \sin(-\beta(t))\sin(-\gamma(t)), \cos(-\beta(t))\}$, which traces out a path on the unit sphere. The QA angles for the PN waveform define $\vec{n}_{\rm PN}(t)$, while those for the NR waveform define $\vec{n}_{\rm NR}(t)$. We perform a fixed rotation $\mathbf{R}_{\rm PN}$ to $\vec{n}_{\rm PN}(t)$ (and another $\mathbf{R}_{\rm NR}$ to $\vec{n}_{\rm NR}(t)$), such that both vectors are equal at the matching frequency, $\vec{n}_{\rm PN}(t_{\rm PN}) = \vec{n}_{\rm NR}(t_{\rm NR})$. Since the angle γ is ill-defined when $\vec{n} = \{0, 0, 1\}$, we do not choose that as our (arbitrary) matching direction, but rather the vector such that $\beta(t_{\rm PN}) = 0.1$ rad. Specification of a third Euler angle allows us to require that the vectors not only meet at the matching time, but that the curves they trace out are parallel at that time. To do this we simply measure the angle between the two curves at the matching time, and then rotate $\vec{n}_{\rm NR}(t)$ around the axis defined by the matching direction, $\vec{n}_{\rm NR}(t_{\rm NR})$. Figure 10 shows the first two angles at the times close to the matching frequency, and the final PN and NR curves are shown in the lower panel of Fig. 10. The hybrid angles are constructed by smoothly blending between the PN and NR angles, in the same way as for the QA waveform. The precessing-binary hybrid can then be constructing by performing the reverse QA procedure with $\{\gamma, \beta, \varepsilon\} \rightarrow \{-\varepsilon, -\beta, -\gamma\}$.

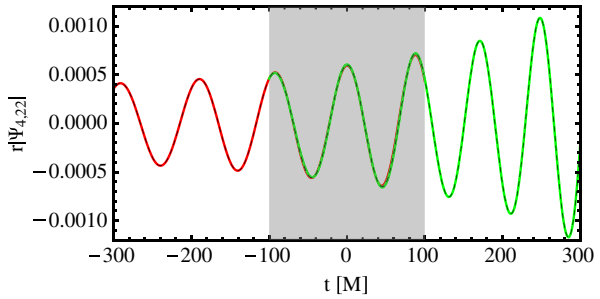

FIG. 9 (color online). The PN (red, from $t = -300M$ to $t = 100M$), NR (green, from $-100M$ to $300M$) and hybrid (dashed black) waveforms near the matching time ($t = 0$). The PN and NR waveforms are blended together in the window $\Delta t = [-100, 100]$, indicated by the shaded region.

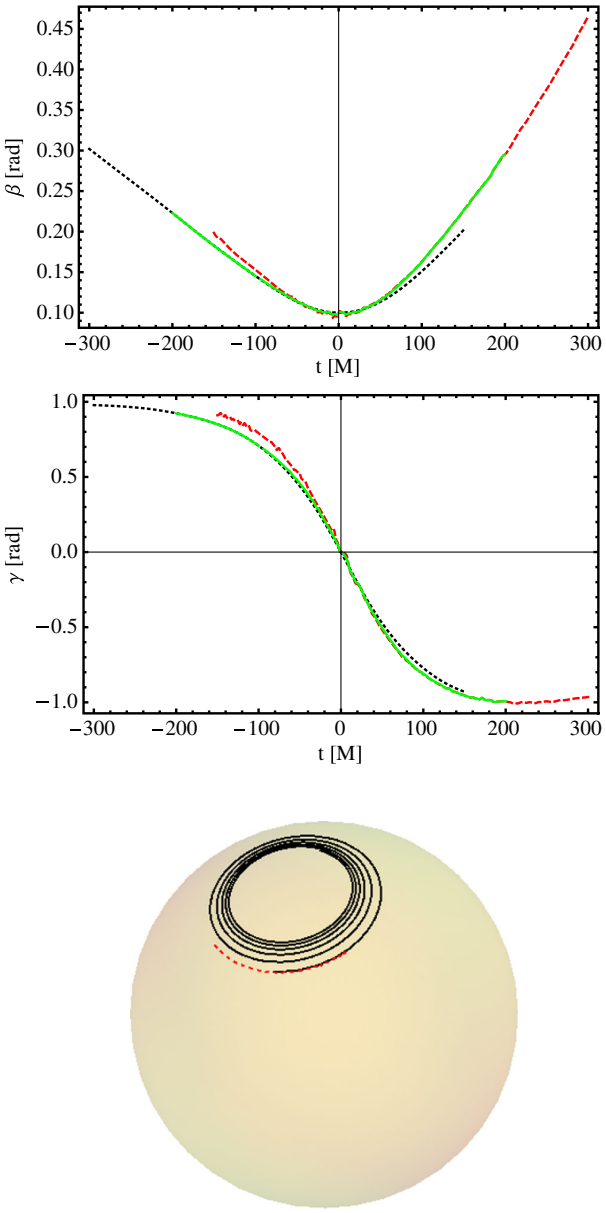

FIG. 10 (color online). Hybridization of the QA angles β and γ. Upper two panels: the black (dotted) lines indicate the inspiral PN values, the red (dashed) lines indicate the later NR values, and the green (solid) lines indicate the hybrids. The lower figure shows the evolution of the aligned QA directions, where here the black line indicates long PN inspiral of duration 2.9×10^5 M, and the red line indicates the NR results up to merger.

B. Breakdown of the nonprecessing-binary equivalence

We expect the simple mapping between QA- and nonprecessing-binary waveforms to break down near merger. As we have seen, the effect of the spins on the inspiral rate comes predominantly from the spin components parallel to the orbital angular momentum; this is why our mapping works. At merger, however, the spin of the final black hole is, to first approximation, $\vec{J}_{\rm fin} = \vec{L} + \vec{S}_1 + \vec{S}_2$, where the orbital and spin angular momentum vectors are those at the point of merger. (A far more sophisticated treatment of the final spin ingredients is given in Ref. [68], and a number of estimates of the final spin as a function of the initial configuration exist in the literature [69–71].) All components of the spin now become important and the appropriate parametrization may no longer be the effective total spin $\chi_{\rm eff}$.

It is instructive to investigate where the mapping breaks down, and we can use the hybrid waveform constructed in the previous section to do this. Figure 11 shows the match between the QA hybrid constructed above, and a nonspinning $q = 3$ hybrid (which would be the appropriate nonprecessing configuration during the inspiral). The match is calculated for a range of termination frequencies of the two waveforms. For reference, the frequency $fM = 0.016$ corresponds roughly to $M\omega = 0.1$, and is close to the point where PN waveforms are typically terminated in inspiral searches. Below this frequency the white-noise match is consistent with the results in Sec. III A. The peak of the waveform occurs at $fM = 0.07$, which is indicated by a vertical line. The fiducial acceptable match of 0.97 is indicated by a horizontal line. We see that the match is at or above 0.97 through the merger and only degrades significantly during the ringdown.

Once again we emphasize that these matches were computed using a white-noise power spectrum. Nonetheless, these provide evidence that the QA procedure is valid very close to the merger, and perhaps even up to ringdown. We will discuss the implications of this result for waveform modeling in the final section.

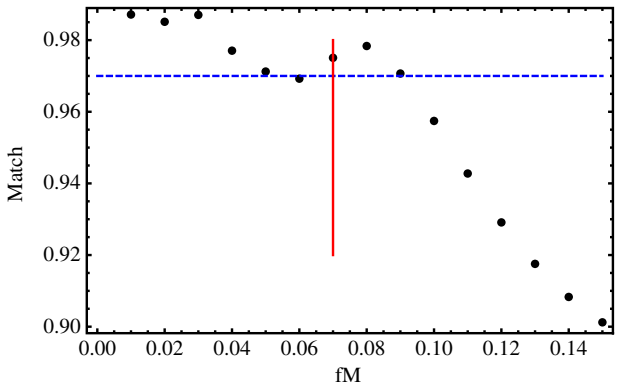

FIG. 11 (color online). Matches between QA and nonprecessing hybrids, for our standard $q = 3$ configuration. The horizontal axis represents the frequency at which both waveforms are cut off in the match calculation, and indicates that the two hybrids agree well (match >0.97) right up to the merger, indicated by the vertical line.

V. DISCUSSION: A ROUTE TO GENERIC BINARY WAVEFORM MODELS

We have extended previous work on the QA procedure to show that it can be used not only to cast precessing-binary waveforms in a simple form, but to map these waveforms onto a subfamily of nonprecessing waveforms. We verified that this subfamily is parametrized by only mass ratio and an effective total spin parameter, and that the nonprecessing waveform that best matches each QA waveform (with white-noise matches of at least 0.995), corresponds to our predicted $\chi_{\rm eff}$-value to within $\Delta\chi \leq 0.04$. The mapping was tested on a range of inspiral PN waveforms with mass ratios $q = 3$ and $q = 10$, and even on an example of transitional precession; in all cases the approximations holds well within the level of accuracy of the PN phasing. As a final test, we used the reverse QA procedure to "wrap up" a nonprecessing-binary waveform, and found that it matched the corresponding true precessing waveform with a match of >0.97 for all binary orientations. We also showed that this procedure can simplify the construction of hybrid PN-NR waveforms, and that the approximate mapping seems to hold all the way through to merger.

Our results suggest that generic precessing-binary waveforms can be generated with good accuracy by applying the reverse of the quadrupole-alignment transformation to a small class of nonprecessing-binary waveforms. These waveforms appear to faithfully represent the "true" precessing-binary waveforms up to the point of merger, and perhaps even up to the ringdown. The problem of constructing a generic waveform model can then be factorized into the smaller problem of modeling the two rotation angles $\{\beta(t), \gamma(t)\}$ as a function of the black-hole spins and the mass ratio.

More concretely, we propose the following strategy: once the evolution of the Euler angles $\beta(t)$ and $\gamma(t)$ has been determined for a large sample of the configuration space, these can be modeled as functions that depend on some set of parameters $\vec{\lambda}$

$$\beta = \beta(\vec{\lambda}(t)), \tag{5.1}$$

$$\gamma = \gamma(\vec{\lambda}(t)). \tag{5.2}$$

We emphasize that the $\vec{\lambda}$ should be *physical* parameters, or a combination of physical parameters. The third angle $\varepsilon(t)$ is automatically determined given the two others. The rotation angles are unique up to an overall rotation of the frame of reference; we expect that they will assume the simplest form if in the limit of infinite binary separation $\hat{J}_{-\infty} = (0, 0, 1)$.

Since precessing inspiral-merger (IM) waveforms can be mapped onto nonprecessing ones via quadrupole alignment,

using the angles $\{\gamma(t), \beta(t), \varepsilon(t)\}$, a phenomenological IM model with (anti-) aligned spins can be used and "twisted up" with the inverse angles $\{-\varepsilon(t), -\beta(t), -\gamma(t)\}$. This will give us a phenomenological IM model,

$$h^{\rm IM}_{lm}(t) = \mathbf{R}(-\varepsilon, -\beta, -\gamma) h^{\rm IM}_{lm}(\eta, \chi_{\rm eff}; t). \quad (5.3)$$

Needless to say, an *inspiral* model is not urgently needed: we can already produce generic waveforms by integrating the PN equations of motion, as we have done in this paper. A simple closed-form approximation to these solutions could significantly improve the efficiency of gravitational-wave search and parameter-estimation pipelines, but there is no barrier in principle to producing theoretical estimates of any of these signals. The real need is for complete IMR waveform models.

Given in addition a phenomenological model for the ringdown, $h^{R}_{\ell m}(\vec{\lambda}_R; t)$, which is parametrized by some yet-to-be-determined subset $\vec{\lambda}_R$ of the full binary parameters $\vec{\lambda}$, we expect that we can produce a combined IMR model, which can be indicated schematically as

$$h^{\rm IMR}_{lm}(t) = \mathbf{R}(-\varepsilon, -\beta, -\gamma) h^{\rm IM}_{lm}(\eta, \chi_{\rm eff}; t) \times h^{R}_{\ell m}(\vec{\lambda}_R; t). \quad (5.4)$$

For ease of use in GW searches, ideally this model would be cast in closed-form expressions in the frequency domain.

We still have the problem of modeling a seven-dimensional parameter space, but we now have to model only two functions, and, as we can see from Fig. 3 (and even Fig. 8 for transitional precession), they are smooth, simple functions, that may be far easier to model than the complicated amplitude and phase modulations that are standard features of the physical waveforms. It is also likely that many of the features of the full seven-dimensional parameter space can be captured by a model that considers only a subset of the parameters. It is also quite possible that we will need to employ a nonprecessing model that treats both black-hole spins, and/or the effective spin that proves most useful will differ from that presented here. Our main purpose is only to outline a general research program to develop generic waveform models based on QA waveforms.

In the short term, a number of issues deserve further study. One is that the QA method, in all forms proposed to date [11,45,46], has only been studied in detail prior to merger. It is likely that in order to apply the QA method optimally through the ringdown, it will be advantageous to make use of spheroidal (rather than spherical) harmonics, but that remains to be seen. Another will be the appropriate blending between the inspiral-merger regime and the ringdown, which is likely to be parametrized by the final mass and spin, and probably also the mass ratio and a second effective spin parameter [72]. It would also be instructive to explore the effectiveness of such signals for both GW searches and parameter estimation across a wide volume of the binary parameter space.

We consider all of these to constitute a promising strategy for the construction of approximate generic waveform models, and will pursue them further in future work.

ACKNOWLEDGMENTS

We thank G. Faye for providing us with a MATHEMATICA notebook containing all waveform-mode expressions used in this work. We also thank P. Ajith, S. Fairhurst, I. Harry, F. Ohme, M. Pürrer and B. Sathyaprakash for discussions and A. Buonanno, E. Ochsner and F. Ohme for comments on the manuscript. P. Schmidt is a recipient of a DOC-FORTE fellowship of the Austrian Academy of Sciences and was also partially supported by the STFC. M. Hannam was supported by Science and Technology Facilities Council Grants No. ST/H008438/1 and No. ST/I001085/1. S. Husa was supported by Grant No. FPA-2007-60220 from the Spanish Ministry of Science and the Spanish MICINNs Consolider-Ingenio 2010 Programme under Grant MultiDark No. CSD2009-00064 and thanks Cardiff University for hospitality. BAM simulations were carried out at Advanced Research Computing (ARCCA) at Cardiff, LRZ Munich, the Vienna Scientific Cluster (VSC), MareNostrum at Barcelona Supercomputing Center—Centro Nacional de Supercomputación (Spanish National Supercomputing Center), and on the PRACE clusters Hermit and Curie.

[1] B. Abbott *et al.* (LIGO Scientific), Rep. Prog. Phys. **72**, 076901 (2009).
[2] D. Shoemaker (the Advanced LIGO Team), Advanced LIGO Reference Design 2009 (LIGO-M060056).
[3] G. M. Harry and the LIGO Scientific Collaboration, Classical Quantum Gravity **27**, 084006 (2010).
[4] T. Accadia, F. Acernese, F. Antonucci, P. Astone, G. Ballardin *et al.*, Classical Quantum Gravity **28**, 114002 (2011).
[5] The Virgo Collaboration, Advanced Virgo Baseline Design 2009 (VIR-0027A-09).
[6] K. Somiya (LCGT Collaboration), Classical Quantum Gravity **29**, 124007 (2012).
[7] J. Abadie *et al.* (LIGO Scientific Collaboration, Virgo Collaboration), Classical Quantum Gravity **27**, 173001 (2010).
[8] F. Ohme, Classical Quantum Gravity **29**, 124002 (2012).

[9] R. Sturani, S. Fischetti, L. Cadonati, G. M. Guidi, J. Healy D Shoemaker, and A Viceré, J. Phys. Conf. Ser. **243**, 012007 (2010).
[10] NRAR, NRAR, https://www.ninja-project.org/doku.php?id=nrar:home.
[11] P. Schmidt, M. Hannam, S. Husa, and P. Ajith, Phys. Rev. D **84**, 024046 (2011).
[12] P. Ajith, M. Hannam, S. Husa, Y. Chen, B. Bruegmann *et al.*, Phys. Rev. Lett. **106**, 241101 (2011).
[13] L. Santamaría *et al.*, Phys. Rev. D **82**, 064016 (2010).
[14] Y. Pan, A. Buonanno, M. Boyle, L. T. Buchman, L. E. Kidder, H. P. Pfeiffer, and M. A. Scheel, Phys. Rev. D **84**, 124052 (2011).
[15] A. Buonanno, Y.-b. Chen, and M. Vallisneri, Phys. Rev. D **67**, 104025 (2003).
[16] L. E. Kidder, Phys. Rev. D **52**, 821 (1995).
[17] P. Ajith, Phys. Rev. D **84**, 084037 (2011).
[18] T. A. Apostolatos, C. Cutler, G. J. Sussman, and K. S. Thorne, Phys. Rev. D **49**, 6274 (1994).
[19] D. A. Brown, A. Lundgren, and R. O'Shaughnessy, Phys. Rev. D **86**, 064020 (2012).
[20] R. O'Shaughnessy, J. Healy, L. London, Z. Meeks, and D. Shoemaker, Phys. Rev. D **85**, 084003 (2012).
[21] S. Husa, M. Hannam, J. A. González, U. Sperhake, and B. Brügmann, Phys. Rev. D **77**, 044037 (2008).
[22] M. Hannam, S. Husa, F. Ohme, D. Muller, and B. Bruegmann, Phys. Rev. D **82**, 124008 (2010).
[23] M. Pürrer, S. Husa, and M. Hannam, Phys. Rev. D **85**, 124051 (2012).
[24] P. Jaranowski and G. Schäfer, Phys. Rev. D **57**, 7274 (1998).
[25] T. Damour, P. Jaranowski, and G. Schäfer, Phys. Lett. B **513**, 147 (2001).
[26] T. Damour, P. Jaranowski, and G. Schäfer, Phys. Rev. D **62**, 021501 (2000).
[27] L. Blanchet and G. Faye, Phys. Rev. D **63**, 062005 (2001).
[28] V. C. de Andrade, L. Blanchet, and G. Faye, Classical Quantum Gravity **18**, 753 (2001).
[29] L. Blanchet and B. R. Iyer, Classical Quantum Gravity **20**, 755 (2003).
[30] L. Blanchet, Classical Quantum Gravity **15**, 113 (1998).
[31] L. Blanchet, B. R. Iyer, and B. Joguet, Phys. Rev. D **65**, 064005 (2002).
[32] L. Blanchet, T. Damour, G. Esposito-Farese, and B. R. Iyer, Phys. Rev. Lett. **93**, 091101 (2004).
[33] B. Barker and R. O'Connell, Phys. Rev. D **2**, 1428 (1970).
[34] B. Barker and R. O'Connell, Gen. Relativ. Gravit. **5**, 539 (1974).
[35] B. Barker and R. O'Connell, Gen. Relativ. Gravit. **11**, 149 (1979).
[36] T. Damour, Phys. Rev. D **64**, 124013 (2001).
[37] E. Poisson, Phys. Rev. D **57**, 5287 (1998).
[38] L. Blanchet, A. Buonanno, and G. Faye, Phys. Rev. D **74**, 104034 (2006).
[39] G. Faye, L. Blanchet, and A. Buonanno, Phys. Rev. D **74**, 104033 (2006).
[40] T. Damour, P. Jaranowski, and G. Schäfer, Phys. Rev. D **77**, 064032 (2008).
[41] A. Buonanno, Y. Chen, and T. Damour, Phys. Rev. D **74**, 104005 (2006).
[42] K. Alvi, Phys. Rev. D **64**, 104020 (2001).
[43] K. Arun, A. Buonanno, G. Faye, and E. Ochsner, Phys. Rev. D **79**, 104023 (2009).
[44] P. Schmidt, M. Hannam, and S. Husa (to be published).
[45] M. Boyle, R. Owen, and H. P. Pfeiffer, Phys. Rev. D **84**, 124011 (2011).
[46] R. O'Shaughnessy, B. Vaishnav, J. Healy, Z. Meeks, and D. Shoemaker, Phys. Rev. D **84**, 124002 (2011).
[47] E. P. Wigner, *Group Theory and its Application to the Quantum Mechanics of Atomic Spectra* (Academic Press Inc., New York, 1959).
[48] J. N. Goldberg, A. J. MacFarlane, E. T. Newman, F. Rohrlich, and E. C. G. Sudarshan, J. Math. Phys. (N.Y.) **8**, 2155 (1967).
[49] M. Hannam *et al.*, Phys. Rev. D **79**, 084025 (2009).
[50] E. Ochsner and R. O'Shaughnessy, arXiv:1205.2287.
[51] C. Cutler and E. E. Flanagan, Phys. Rev. D **49**, 2658 (1994).
[52] D. Shoemaker and G. Losurdo, LIGO Project, Tech. Rep. No. LIGO-G10001760-v7, 2010, https://dcc.ligo.org/DocDB/0009/G1000176/007/Advanced%20Virgo%20and%20LIGO%20post-project%20progression.pdf.
[53] The LIGO Scientific Collaboration, LIGO Project, Tech. Rep. No. LIGO-T0900288-v3, 2009, https://dcc.ligo.org/DocDB/0002/T0900288/003/AdvLIGO%20noise%20curves.pdf.
[54] P. Ajith, M. Boyle, D. A. Brown, B. Brugmann, L. T. Buchman *et al.*, Classical Quantum Gravity **29**, 124001 (2012).
[55] Y. Pan, A. Buonanno, J. G. Baker, J. Centrella, B. J. Kelly, S. T. McWilliams, F. Pretorius, and J. R. van Meter, Phys. Rev. D **77**, 024014 (2008).
[56] P. Ajith *et al.*, Classical Quantum Gravity **24**, S689 (2007).
[57] P. Ajith *et al.*, Phys. Rev. D **77**, 104017 (2008).
[58] M. Boyle, D. A. Brown, and L. Pekowsky, Classical Quantum Gravity **26**, 114006 (2009).
[59] M. Hannam, S. Husa, F. Ohme, and P. Ajith, Phys. Rev. D **82**, 124052 (2010).
[60] P. Ajith, Classical Quantum Gravity **25**, 114033 (2008).
[61] I. MacDonald, S. Nissanke, H. P. Pfeiffer, and H. P. Pfeiffer, Classical Quantum Gravity **28**, 134002 (2011).
[62] M. Boyle, Phys. Rev. D **84**, 064013 (2011).
[63] F. Ohme, M. Hannam, and S. Husa, Phys. Rev. D **84**, 064029 (2011).
[64] M. Hannam, S. Husa, B. Brügmann, J. A. González, and U. Sperhake, Classical Quantum Gravity **24**, S15 (2007).
[65] G. Lovelace, Classical Quantum Gravity **26**, 114002 (2009).
[66] M. Hannam, S. Husa, D. Pollney, B. Brügmann, and N. Ó Murchadha, Phys. Rev. Lett. **99**, 241102 (2007).
[67] M. Hannam, S. Husa, F. Ohme, B. Brügmann, and N. Ó Murchadha, Phys. Rev. D **78**, 064020 (2008).
[68] A. Buonanno, L. E. Kidder, and L. Lehner, Phys. Rev. D **77**, 026004 (2008).
[69] L. Rezzolla, P. Diener, E. N. Dorband, D. Pollney, C. Reisswig, E. Schnetter, and J. Seiler, Astrophys. J. **674**, L29 (2008).
[70] W. Tichy and P. Marronetti, Phys. Rev. D **78**, 081501 (2008).
[71] C. O. Lousto, M. Campanelli, and Y. Zlochower, Classical Quantum Gravity **27**, 114006 (2010).
[72] I. Kamaretsos, M. Hannam, and B. Sathyaprakash, Phys. Rev. Lett. **109**, 141102 (2012).